

DOI: 10.54503/0571-7132-2023.66.2-195

MULTIWAVELENGTH PROPERTIES OF SELECTED
HIGH REDSHIFT BLAZARSG.HARUTYUNYAN^{1,2}

Received 15 March 2023

Accepted 22 May 2023

High-redshift blazars detected in the γ -ray band are the most powerful steady objects in the universe. Multiwavelength observations of these distant objects are of particular interest as they can help to understand the γ -ray evolution of blazars as well as the formation and propagation of relativistic jets in the early epochs of the Universe. In this study, we investigate the origin of broadband emission from 7 blazars with redshifts greater than 2.5 by analyzing the data accumulated with Swift UVOT/XRT and Fermi-LAT. We observe several flaring periods with significant increases in flux and hardening of the photon index in the high-energy γ -ray band for PKS 1830-211 ($z = 2.507$), LQAC 247-061 ($z = 2.578$), TXS 0536+145 ($z = 2.690$), and 4C+41.32 ($z = 2.550$). PKS 1830-211 was in an extraordinarily bright state on MJD 58596.49 when the 3-day averaged flux increased up to $(1.74 \pm 0.04) \cdot 10^{-5}$ photon $\text{cm}^{-2} \text{s}^{-1}$. The X-ray emission of PKS 1830-211 is also strongly variable and is characterized by a hard photon index in the range of 0.34–0.94. To model the time-averaged broadband spectral energy distribution of the considered sources, we used a one-zone leptonic emission mechanism for the inverse Compton scattering, considering both synchrotron and external photons. We estimated the corresponding parameters of the emitting particles as well as the energetics of the jet.

Keywords: *radiation mechanisms: non-thermal: X-rays: gamma-rays: blazars*

1. *Introduction.* Blazars belong to the subclass of active galactic nuclei which have a jet that is making small angle in respect with the observer. The emission from blazars is observed in a broad range from radio to high energy (HE; >100 MeV) γ -ray bands [1]. This emission is most likely produced in a compact emitting region and is characterized by fast and significant variability in almost all wavelengths, with the most rapid changes occurring in the γ -ray band, often being order of minutes (e.g., [2-10]). A recent review by Padovani et al. [1] provides more information on blazars and their multiwavelength emission properties.

Blazars are typically classified into two subcategories: flat-spectrum radio quasars (FSRQs) and BL Lacertae objects [11]. FSRQs have strong broad emission lines in their optical spectrum, while BL Lacs show weak or no lines. The broadband spectral energy distribution (SED) of blazars has two broad peaks [1]. The low-energy component, which usually is explained as synchrotron emission by relativistic electrons, has a peak between the infrared and X-ray bands, and this peak is used to further categorize blazars as low, intermediate, or high

synchrotron peaked sources based on their synchrotron peak frequency ν_s in the rest frame. When $\nu_s < 10^{14}$ Hz, blazars are referred to as low synchrotron peaked (LSP) sources, while intermediate synchrotron peaked (ISP) and high synchrotron peaked (HSP) sources have ν_s values between 10^{14} and 10^{15} Hz and $>10^{15}$ Hz, respectively [12,13].

Various models have been proposed to explain the double-peaked SED of blazars. While it is widely agreed that the low-energy component is due to the synchrotron radiation of electrons, the origin of the second component is a topic of ongoing debate. In conventional leptonic scenarios, this component is produced when synchrotron-emitting electrons inverse Compton scatter either internal photons (synchrotron self-Compton (SSC) [14-16]) or external photons (external inverse Compton (EIC) [17-19]). The nature of the external photon fields depends on the location of the emitting region, and can be dominated by photons directly emitted from the accretion disk [20,21], disk photons reflected from the broad-line region (BLR; [19]) or IR photons emitted from the dusty torus [17]. Recently, after the association of TXS 0506+056 with the IceCube-170922A neutrino event [22,23], the models involving energetic protons to explain the second component in the SED have become more favorable. The HE component can be caused by either proton synchrotron emission [24] or secondary particles resulting from pion decay [24-28]. In these hadronic or lepto-hadronic scenarios, also emission of very high energy neutrinos is expected [23,29-37].

Blazars are the dominant sources in the extragalactic γ -ray sky. Because of the relativistic amplification of their emission, sources even at high redshift are observed. For example, the Fermi Large Area Telescope (LAT) 12-Year Point Source Catalog (data release 3 (DR3) [38]) contains 38 blazars detected beyond $z=2.5$ and 11 beyond $z=3.0$. The investigation of the multiwavelength properties of these high redshift blazars is especially important as they are the most powerful non-explosive astrophysical sources and their study can be crucial for understanding the jet formation and propagation around supermassive black holes.

Table 1

LIST OF γ -RAY EMITTING BLAZARS WITH REDSHIFT BEYOND 2.5

Associated name	4FGL name	Class	z
PKS 1830-211	J1833.6-2103	FSRQ	2.507
LQAC 247-061	J1628.8-6149	FSRQ	2.578
4C +41.32	J1625.7+4134	FSRQ	2.550
PKS 2311-452	J2313.9-4501	BCU	2.884
PMN J0833-0454	J0833.4-0458	FSRQ	3.450
PKS 2318-087	J2320.8-0823	FSRQ	3.164
TXS 0536+145	J0539.6+1432	FSRQ	2.690

Sahakyan et al. [39] have already studied the multiwavelength characteristics of the majority of high redshift blazars (33) detected in the HE γ -ray band, with a redshift greater than 2.5. The selection of high redshift blazars in Sahakyan et al. [39] was based on the first eight years of Fermi-LAT observations, while the most recent available Fermi-LAT catalogue is now based on 12 years of data. Therefore, there are additional 7 sources which are newly classified as high redshift blazars. The list of these objects is given in Table 1, providing for each source its name, 4FGL associated name, its type and redshift. In order to investigate the multiwavelength properties of these newly classified high redshift blazars, the data accumulated from their observations in the optical/UV, X-ray and γ -ray bands was analyzed, and the results were modeled within a leptonic scenario.

The paper is structured as follows: The data analysis is presented in Section 2, the SED modeling and results are given in Section 3 and Summary is provided in Section 4.

2. Data analysis. In the γ -ray band the selected sources were continuously monitored with Fermi-LAT since 2008. Also, they were observed multiple times in the optical/UV and X-ray bands with Swift telescope. All the available data in the mentioned bands were analyzed to investigate the multiwavelength properties of the selected sources.

2.1. Fermi-LAT data analysis. Onboard the Fermi Gamma-ray Space Telescope, the Large Area telescope (LAT) is a pair-conversion telescope operating in the energy range from 30 MeV to 500 GeV. It scans the entire sky every ~ 3 hours, continuously monitoring the γ -ray emission from Galactic and extragalactic sources. More details on the LAT instrument are given in Atwood et al. 2009 [40].

In the current study, the data accumulated between 2008 August 04 and 2022 December 04 (MET 239557417-691804805) were analyzed using the standard Fermi Science Tools version 1.2.1. The data was processed using the P8R3_SOURCE_V3 instrument response function for the PASS 8 data. The events in the energy range from 100 MeV to 500 GeV were downloaded from a 12° region of interest (ROI) centered on the position of each source. In *gtselect* tool with a filter of "evclass = 128, evtype = 3", only the events which have high probability of being photons were selected. Also, a filter of a zenith angle of $>90^\circ$ was applied to remove contamination by photons from Earth's atmosphere. In the *gtmktime* tool a filter of "(DATAQUAL > 0) &&(LATCONFIG == 1)" was applied to select good time intervals. Then the events are binned into a $16^\circ.9 \times 16^\circ.9$ square region into pixels of $0^\circ.1 \times 0^\circ.1$ and into 37 equal logarithmically spaced energy bins with *gtbin* tool. For each source, a model file describing the sources included in the region of interest was created using the Fermi-LAT fourth source

catalog Data Release 3 (4FGL-DR3) [38]. The significance of the source detection is quantified using test statistics TS defined as $TS = 2\log(L_1/L_0)$, where L_0 and L_1 are the likelihoods of the model without source (null hypothesis) and alternative likelihood (with source), respectively. The model file includes all the sources within $ROI+5^\circ$ around the targets; the spectral parameters of the other sources within the ROI were left free, while those outside the ROI were fixed to their catalog values. The model file includes also diffuse and isotropic backgrounds, which were modeled with standard *gll_iem_v07* and *iso_P8R3_SOURCE_V3_v1* models with the normalization considered as a free parameter. The entire data was initially analyzed using a binned maximum likelihood analysis implemented in *gtlike* tool.

After analyzing the data from the entire period, the γ -ray variability of the selected sources was investigated. Initially, the whole time period was divided into short equal periods and the unbinned likelihood analysis was applied to estimate the flux and the photon index. The duration of the time bin was selected based on the overall detection significance of the source. In general, several tens of days were selected to ensure that periods with source detection exceeded the periods for which only upper limits were observed. As a next step, in order to better investigate the evaluation of γ -ray flux in time, the light curves were computed with the help of the adaptive binning method. In this approach, the time bin widths are non-equal and are defined by requiring a constant relative flux uncertainty. This implies that during the low-flux state the time bins are wider, and they are narrower when the source is in a flaring state. So, these light curves are informative, allowing to investigate the flux variations in short time scales and identify flaring periods [41-44,7].

The γ -ray light curves of selected sources are shown in Fig.1. For each source, when the light curve generated with the adaptive binning method is with reasonable time bins, the light curves generated with fixed bins (circle) and with adaptive bins are shown. The light curves for PKS 1830-211 and LQAC 247-061 were downloaded from the Fermi-LAT Light Curve Repository, as the ROI around these sources contains a lot of objects, making the analysis difficult. The most variable source in the sample is PKS 1830-211 (Fig.1a) which shows high amplitude flux changes in the 3-day binned light curve. The γ -ray emission of this source increases time to time but the largest flare was observed during MJD 58572-58605 when the flux increased up to $(1.74 \pm 0.04) \cdot 10^{-5}$ photon $\text{cm}^{-2} \text{s}^{-1}$ on MJD 58596.49. It should be noted that the average flux of γ -ray emission from this source is $(1.01 \pm 0.19) \cdot 10^{-6}$ photon $\text{cm}^{-2} \text{s}^{-1}$, so the flux increases ~ 17.22 times. The time-averaged γ -ray spectrum of PKS 1830-211 is well explained with the index of $\Gamma_\gamma = 2.66 \pm 0.34$ but during the brightening the hardest index of $\Gamma_\gamma = 2.22 \pm 0.03$ was observed on MJD 58596.49. The γ -ray light curve of LQAC

247-061 with 7-day bins shows (Fig.1b) several flaring periods although with smaller amplitudes as compared to PKS 1830-211: the maximum weekly flux of this source was $(5.87 \pm 1.34) \cdot 10^{-7}$ photon $\text{cm}^{-2} \text{s}^{-1}$ observed on MJD 59222.42. The adaptively binned light curve of TXS 0536+145 above 285.38 MeV (Fig.1c) shows that the source was in an active emission state between MJD 55872-56138 when the flux above 285.38 MeV increased up to $(1.81 \pm 0.39) \cdot 10^{-7}$ photon $\text{cm}^{-2} \text{s}^{-1}$ on MJD 55945.22. On average, the γ -ray spectral index of this source is around $\Gamma_{\gamma} = 2.68$ but during the flares occasionally it hardens, for example, on MJD 56014.81 the index was $\Gamma_{\gamma} = 2.00 \pm 0.16$. Among the considered sources, the light curve generated with the help of the adaptive binning method shows that 4C+41.32 also has a variable γ -ray emission (Fig.1d); the averaged γ -ray flux of the source was $(3.24 \pm 0.94) \cdot 10^{-9}$ photon $\text{cm}^{-2} \text{s}^{-1}$ which increased up to $(5.75 \pm 0.12) \cdot 10^{-9}$ photon $\text{cm}^{-2} \text{s}^{-1}$ on MJD 56177.66. It should be noted that during this bright period the photon index hardened to $\Gamma_{\gamma} = 2.10 \pm 0.11$. For the other remaining three sources (PKS 2311-452, PKS 2318-087 and PMN J0833-0454), no flux changes

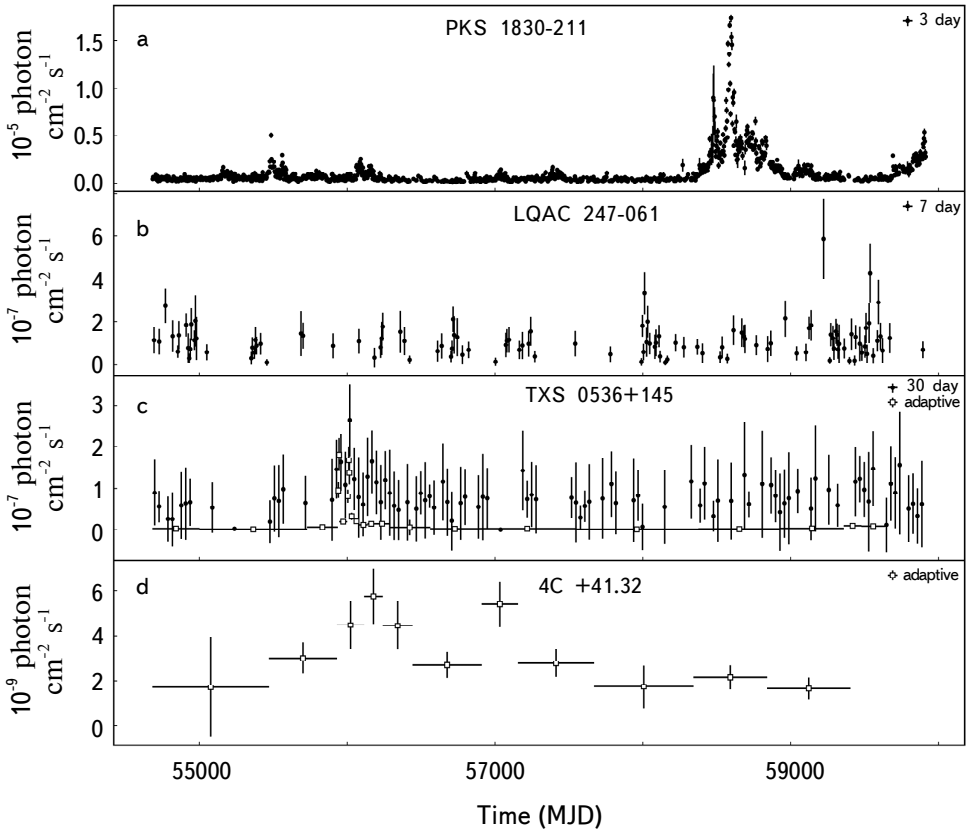


Fig.1. The γ -ray light curve of selected sources. The light curves generated with the help of adaptive binning are shown as empty squares while solid circles are regular/normal time binning.

were observed in long- and short-time scales.

2.2. Swift observations of selected sources. With three instruments - UVOT, XRT and BAT, the Swift satellite launched in 2004 is a good instrument to study the multiwavelength emission from blazars because of its wide energy coverage. These observations are especially crucial for high redshift blazars which typically have the peak of the HE component at the sub-MeV band, so the X-ray observations can help to constrain the increasing spectrum of the HE component.

Among the considered sources, TXS 0536+145, PMN J0833-0454, LQAC 247-061 and PKS 1830-211 have at least once been observed with the Swift satellite. All the data acquired from the XRT and UVOT observations were downloaded and analyzed. The XRT data were all processed using the *Swift_xrtproc* automatic tool [45]. This tool automatically downloads the Swift data either from SSDC archive¹ or from Swift UK archive² and processes them applying the standard analysis methods. In particular, the Level1 raw data was processed using the XRTPIPELINE script, which included reduction, calibration and cleaning of the data, using standard filtering criteria and the latest CALDB calibration files. The sources' counts were obtained from a circular region of a 20-pixel radius (47") centered on the sources' position, while background counts were taken from an annular ring centered at the source. Finally, the ungrouped data was loaded into XSPEC version 12.11 for spectral fitting, where the source spectrum was modeled as a power-law with Galactic absorption column density obtained from the N_H HEASARC tool³ [46-48].

The Swift XRT data analysis results are presented in Table 2. TXS 0536+145 and LQAC 247-061 each have only 3 observations when the count rate was above 20, so the spectral analysis was executed, and PMN J0833-0454 has only 2. The 2.0-10 keV X-ray flux of PMN J0833-0454 is at the level of $1.86 \cdot 10^{-13} \text{ erg cm}^{-2} \text{ s}^{-1}$, instead, the spectral index is $\Gamma_x = 1.90 \pm 0.53$ and $\Gamma_x = 2.17 \pm 0.47$ which is unusually soft for FSRQs. However, it should be noted that the peak of the synchrotron component of PMN J0833-0454 at higher frequencies is 10^{14} - 10^{15} Hz, which is not typical for FSRQs. Similarly, the 2.0-10 keV X-ray flux of TXS 0536+145 and LQAC 247-061 is $(0.91 - 2.28) \cdot 10^{-12} \text{ erg cm}^{-2} \text{ s}^{-1}$ and $(1.00 - 1.79) \cdot 10^{-12} \text{ erg cm}^{-2} \text{ s}^{-1}$, respectively, and their indices are 1.45-1.88 and 1.05-1.39, respectively. PKS 1830-211 is the most variable source in the X-ray band; the variation of 2.0-10 keV X-ray flux and photon index is shown in Fig.2. In different observations the change of the flux is evident, the highest flux of

¹ <https://www.ssd.csi.it>

² <https://www.swift.ac.uk/archive/>

³ <https://heasarc.gsfc.nasa.gov/cgi-bin/Tools/w3nh/w3nh.pl>

Table 2

SWIFT XRT ANALYSIS RESULTS

Object	Observation ID	Date	$F_{(2.0-10)}$ keV ¹	Index	C-Stat(d.o.f.)
PMN J0833-0454	00034962002	2017-12-13	0.17±0.37	2.17±0.47	0.98(34)
PMN J0833-0454	00034962003	2017-12-17	0.19±0.23	1.91±0.53	0.87(26)
LQAC 247 -061	00085339012	2015-05-08	1.78±0.7	1.05±0.47	0.83(37)
LQAC 247 -061	00085339014	2015-05-13	1.36±0.47	1.39±0.36	0.88(55)
LQAC 247 -061	00085339020	2015-06-03	1.02±0.38	1.08±0.4	0.77(55)
TXS 0536+145	00032331001	2012-04-04	2.28±0.6	1.49±0.32	1.14(75)
TXS 0536+145	00032331002	2012-04-18	0.91±0.4	1.88±0.36	0.99(58)
TXS 0536+145	00032331003	2012-11-15	1.4±0.6	1.45±0.31	0.62(79)
PKS 1830-211	00081222001	2015-04-25	17.01±2.12	0.64±0.08	1.77(461)
PKS 1830-211	00038422024	2016-05-18	16.68±2.0	0.57±0.09	1.56(438)
PKS 1830-211	00038422016	2016-04-19	18.55±1.85	0.54±0.1	1.23(424)
PKS 1830-211	00038422022	2016-05-06	17.79±1.85	0.66±0.1	1.57(390)
PKS 1830-211	00038422028	2016-06-05	15.69±1.65	0.55±0.11	1.22(374)
PKS 1830-211	00038422014	2010-10-27	17.27±3.15	0.54±0.11	1.37(357)
PKS 1830-211	00038422021	2016-05-04	18.81±2.19	0.53±0.11	1.7(354)
PKS 1830-211	00038422023	2016-05-11	17.64±1.61	0.6±0.11	1.29(348)
PKS 1830-211	00038422070	2019-06-02	16.94±1.84	0.64±0.12	1.39(347)
PKS 1830-211	00038422013	2010-10-26	15.51±1.69	0.62±0.11	1.38(347)

¹ XRT flux in units of 10^{12} erg cm^{-2} s^{-1}

$(2.41 \pm 0.44) \cdot 10^{-11}$ erg cm^{-2} s^{-1} was observed on MJD 58583.10. The spectral index in the X-ray band is relatively hard, changing from 0.34 ± 0.14 to 0.94 ± 0.25 (lower panel in Fig.2), so it defines the rising spectrum of the HE component.

Along with XRT observations, the considered sources were observed also in the optical/UV bands with the UVOT instrument. The Swift-UVOT data in six different filters, including three optical (*V*, *B*, and *U*) and three ultraviolet (W1, M2, and W2), was processed using the latest version of HEASoft, 6.29, and the HEASARC CALDB. A 5-arcsec radius region centered at the source was used to extract the source counts, while the background counts were obtained from a region of 20-arcsec radius located away from the source. The *uvotsource* tool was used to determine the magnitude of the data, which was then corrected for the effects of reddening and galactic extinction, using the $E(B - V)$ reddening coefficient available from the Infrared Science Archive⁴. Among the considered sources, TXS 0536+145, PMN J0833-0454 and LQAC 247-061 are relatively weak in the optical/UV bands and no measurements are available.

Instead, from PKS 1830-211, even being observed more than 90 times at its position of RA = 278.42, Dec = -21.06, no significant counts are observed, however

⁴ <http://irsa.ipac.caltech.edu/applications/DUST/>

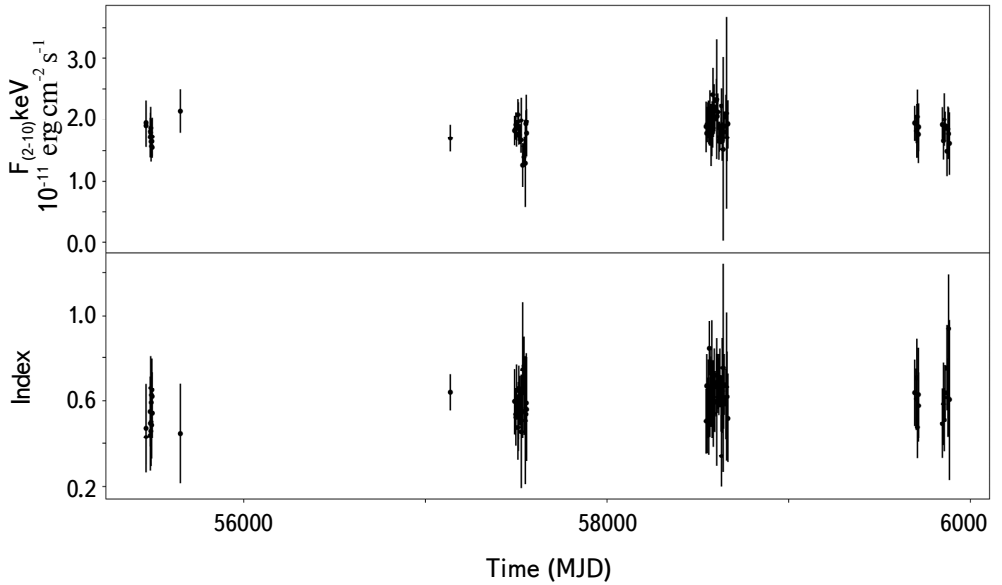


Fig.2. The variation of 2.0-10 keV X-ray flux and 0.3-10.0 keV X-ray photon index of PKS 1830-211.

a significant source at the position of RA = 278.42, Dec = -21.059 is present; however, no obvious association with PKS 1830-211 is available. Considering the complex nature of PKS 1830-211 and the region of the sky (it is possible microlensing/milli-lensing substructures with two foreground lensing galaxies), in order to avoid possible miss-association of the UVOT observations, we dropped the UVOT data for this object.

3. Modeling of multiwavelength SEDs. In order to investigate the origin of broadband emission from the considered sources, the data analyzed here were combined with the archival data retrieved using VOU-blazar tool [49]. This tool accesses over 70 catalogs and databases world-wide and returns all the available multifrequency data. The SEDs composed with data retrieved from VOU-blazar tool and analyzed here, are shown in Fig.3. Since no X-ray measurements are available for PKS 2311-452 and PKS 2318-087, they were not considered during the modeling.

All the considered sources show the characteristic double peaked structure which is modeled within a leptonic one-zone scenario. In this scenario, the electrons are injected and interact with a spherical region of radius R . The emitting region contains a tangled magnetic field of intensity B . This magnetized region moves along the jet with a bulk Lorentz factor of Γ_{jet} making an angle of θ relative to the observer's line of sight.

For a small viewing angle, the emission is amplified by a beaming factor of $\Gamma_{jet} = \delta$. It is assumed that the emitting electrons have a power-law with an exponential cutoff energy distribution in the form of

$$N(\gamma_e) = N_0 \gamma_e^{-p} \exp(-\gamma_e/\gamma_{cut}), \quad \gamma_e > \gamma_{min} \quad (1)$$

where p is the power-law index of electrons, γ_{cut} is the cut-off energy and γ_{min} is the minimal energy. The total electron energy (consequently, N_0 as well) is considered as a free parameter during the fitting.

In this interpretation, the first peak in the SED is accounted for by synchrotron radiation produced as a result of the interaction between the relativistic electrons and the magnetic field within the emitting region. The second peak, ranging from X-rays to HE γ -rays, arises from the inverse Compton scattering of synchrotron (SSC [14-16]) and broad line region (BLR [50,51]) photons. The BLR is modeled as a spherical shell with a lower boundary of $R_{in} = 0.9 R_{BLR}$ and an outer boundary of $R_{in} = 1.2 R_{BLR}$ where $R_{BLR} = 10^{17} L_{BLR} / 10^{45} \text{ erg s}^{-1}$ [52]. It is assumed that L_{BLR} corresponds to 10% of the disk luminosity L_{disk} . The disk emission is approximated as a mono-temperature black body which is estimated by modeling the blue bump in the optical/UV band, if visible. An upper limit is derived by ensuring that the disk emission does not exceed the non-thermal emission observed from the jet, when the additional UV component is not distinguished.

During the SED modeling the free parameters to estimate are N_0 , p , γ_{min} , γ_{cut} , δ , R and B . These parameters were optimized, i.e., to find the optimal values of the parameters best describing the data, the publicly available code JetSet was used [53-56].

3.1. *Results of modeling.* The SEDs modeled with the synchrotron/SSC plus external Compton scattering of BLR photons are shown in Fig.3, and the corresponding parameters are given in Table 3, where the column 1 is the object name, 2 and 3 - the Lorentz factors corresponding to the minimum ($\times 10^2$) and cutoff energy ($\times 10^3$) of the electron distribution, respectively, 4 - magnetic field

Table 3

PARAMETERS OBTAINED FROM THE MODELING OF
MULTIWAVELENGTH SEDs

Sources	γ_{min}	γ_{cut}	B (G)	α	δ	L_d	t_{var}	L_e	L_B
PKS 1830-211	7.53±0.32	5.99±0.41	0.11±0.0	1.79±0.08	13.8±0.31	0.55	9.23	30	0.07
LQAC 247-061	0.27±0.03	2.75±0.27	15.82±1.74	1.97±0.08	12.28±0.84	9.00	2.18	0.21	55
TXS 0536+145	1.33±0.07	12.94±1.82	3.92±0.21	2.96±0.06	14.27±0.63	0.34	3.66	0.68	16
4C +41.32	3.23±0.56	1.62±0.14	0.32±0.03	1.74±0.21	12.32±0.77	0.01	37.3	2.05	6.58
PMN J0833-0454	0.69±0.06	8.57±0.76	9.44±0.91	2.49±0.07	14.58±1.01	0.8	2.60	0.21	33.8

in units of G, 5 - slope of electron energy distribution, 6 - Doppler factor, 7 - accretion disk luminosity L_d in units of $10^{46} \text{ erg s}^{-1}$, 8 - variability time in unit of 10^{-1} day, 9 and 10 - the power of the jet in the form of the relativistic electrons L_e , and magnetic field L_B in units of $10^{45} \text{ erg s}^{-1}$ and $10^{46} \text{ erg s}^{-1}$. The presented SEDs have sufficient data spanning from radio (archival) to HE γ -ray bands (analyzed here), allowing to shape both low- and high-energy peaks. The model utilized is able to effectively explain the multiwavelength data for nearly all of the sources.

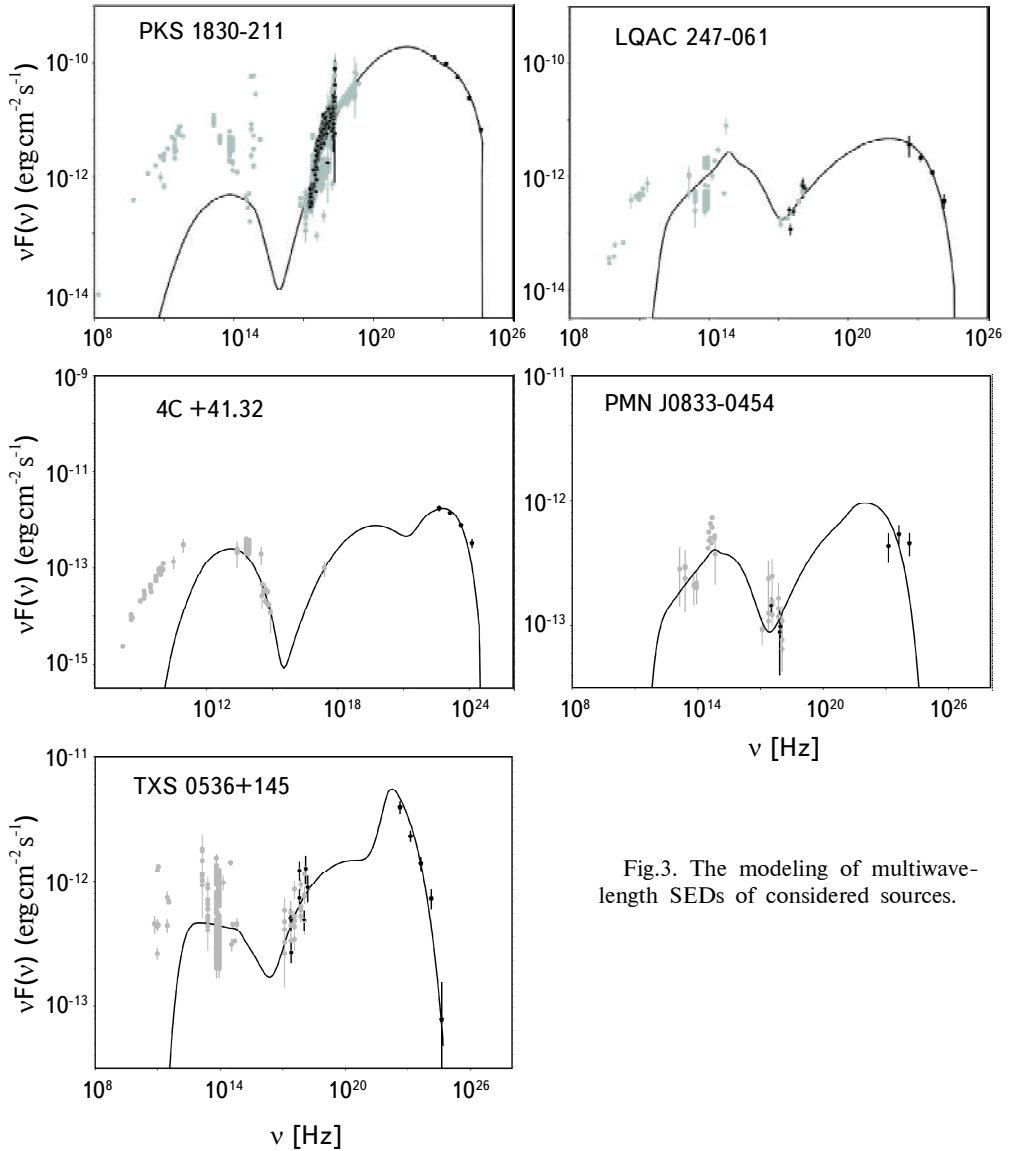


Fig.3. The modeling of multiwavelength SEDs of considered sources.

There is discrepancy for PKS 1830-211, the low-energy data are underestimated by the applied model. However, 1) the region around this source is rather complex, so maybe some of the data are contaminated by the contribution from other sources and 2) the magnetic field and electron content (both affecting the synchrotron component) are strongly constrained by the X-ray and γ -ray data, so the increase of the synchrotron component will imply discrepancy with the X-ray and γ -ray data. The modeling shows that the multiwavelength data of PKS 1830-211, LQAC 247-061 and 4C+41.32 can be explained when the power-law index of emitting electrons is relatively hard, 1.79 ± 0.08 , 1.97 ± 0.08 , 1.74 ± 0.21 , respectively. Whereas, a soft index of correspondingly 2.96 ± 0.06 and 2.49 ± 0.07 is required to explain the data of TXS 0536+145 and PMN J0833-0454. Because of this soft index, the fit resulted in a higher value for the cut-off energy for those two sources - $(12.94 \pm 1.82) \cdot 10^3$ and $(8.57 \pm 0.76) \cdot 10^3$, respectively. The cut-off energy is estimated to be $(5.99 \pm 0.41) \cdot 10^3$, $(2.75 \pm 0.27) \cdot 10^3$ and $(1.62 \pm 0.14) \cdot 10^3$ for PKS 1830-211, LQAC 247-061 and 4C+41.32, respectively. The modeling shows that the magnetic field in the emitting region is within 0.1-15.8 G, where the lowest magnetic field of 0.1 ± 0.01 G is estimated for PKS 1830-211, while the maximum of 15.82 ± 1.74 - for LQAC 247-061. For the considered sources, the Doppler boosting factor varies in a small range of 12.28-14.58 which is a typical value usually estimated for the FSRQs. The modeling allowed to estimate also the variability time or the size of the emitting region. The variability time is of the order of sub-day scales for all the considered sources, except for 4C+41.31, for which $t_{var} = 3.73$ days which corresponds to $R = 3.37 \cdot 10^{16}$ cm, considering its redshift of $z = 2.55$.

By applying the model, it is possible to evaluate the luminosity of the jet. The jet power carried by the electrons and magnetic field is computed using the relations $L_e = \pi c R_b^2 \Gamma^2 U_e$ and $L_B = \pi c R_b^2 \Gamma^2 U_B$, respectively. The corresponding values are given in Table 3. For all the considered sources, the jet is particle-dominated with $L_e/L_B > 1$. The highest total luminosity of $L_{tot} = L_e + L_B = 3.17 \cdot 10^{46}$ erg s⁻¹ is estimated for PKS 1830-211, while PMN J0833-0454 has the lowest luminosity of $5.52 \cdot 10^{44}$ erg s⁻¹. The modeling allows to put an upper limit on the disk luminosity, requiring that it does not overproduce the synchrotron component. The disc luminosity varies in the range of $(0.01 - 9) \cdot 10^{46}$ erg s⁻¹.

4. *Summary.* High redshift blazars are often studied in different bands, providing substantial information on the processes responsible for particle acceleration as well as on the properties of the jet plasma close to supermassive black holes. The high redshift blazars observations in the HE and very high energy γ -ray bands is also important, as they may provide information on the density of extragalactic background light. Up to now, 38 blazars are observed beyond the

redshift of 2.5 which is sufficient enough to have an in-depth view of the processes taking place in these extreme objects.

In the current paper, the multiwavelength emission properties of 7 high redshift blazars are investigated by analyzing the Fermi-LAT and Swift XRT/UVOT data accumulated between 2008 and 2022. The main findings can be summarized as follows:

- The γ -ray emission from PKS 1830-211, LQAC 247-061, TXS 0536+145 and 4C+41.32 varies in time. In the γ -ray band, the most variable source is PKS 1830-21 showing multiple periods of flux enhancement; the brightest flare was observed on MJD 58596.49 when the flux increased up to $(1.74 \pm 0.04) \cdot 10^{-5}$ photon $\text{cm}^{-2} \text{s}^{-1}$.

- In several occasions the γ -ray spectral index of the considered sources hardened significantly. For example, on MJD 56014.81 the index of TXS 0536+145 was $\Gamma_{\gamma} = 2.00 \pm 0.16$ or $\Gamma_{\gamma} = 2.10 \pm 0.11$ index was observed for 4C+41.32 on MJD 56177.66.

- The most variable source in the X-ray band is PKS 1830-211. Its 2.0-10 keV flux increased up to $(2.41 \pm 0.44) \cdot 10^{-11}$ erg $\text{cm}^{-2} \text{s}^{-1}$ on MJD 58583.10 and the X-ray photon index is very hard, varying in the range of 0.34-0.94.

- The multiwavelength emission of PKS 1830-211, LQAC 247-061, TXS 0536+145, 4C+41.32 and PMN J0833-0454 was modeled within a one-zone leptonic scenario considering the Inverse Compton scattering of both synchrotron and BLR photons. The power-law index of the emitting electrons is in the range of 1.79-2.96, the cut-off energy in $(1.62 - 12.94) \cdot 10^3$ and the magnetic field in the emitting region is within 0.11-15.82.

- The modeling allowed to estimate the energetics of the jet of the considered sources. The total jet luminosity varies in the range of $(0.05 - 3.17) \cdot 10^{46}$ erg s^{-1} and the disc luminosity (upper limit) is in the range of $(0.01 - 9) \cdot 10^{46}$ erg s^{-1} .

Acknowledgements. I would like to thank N.Sahakyan and S.Gasparyan for helpful discussions and constructive suggestions. This work was supported by the Science Committee of RA, in the frames of the research project No 21T-1C260.

¹ ICRANet Armenia Marshall Baghramian Avenue 24a, 0019 Yerevan, Republic of Armenia, e-mail: gevorgharutyunyan97@gmail.com

² V.A.Ambartsumian Byurakan Astrophysical Observatory, Armenia

МНОГОВОЛНОВЫЕ СВОЙСТВА ИЗБРАННЫХ
БЛАЗАРОВ С БОЛЬШИМ КРАСНЫМ СМЕЩЕНИЕМ

Г. АРУТЮНЯН

Блазары с большим красным смещением, обнаруженные в γ -диапазоне, являются самыми мощными устойчивыми объектами во Вселенной. Многоволновые наблюдения за этими далекими объектами особенно интересны, так как они могут помочь понять эволюцию γ -излучения блазаров, а также формирование и распространение релятивистских струй в ранние эпохи Вселенной. В данном исследовании мы рассматриваем происхождение широкополосной эмиссии 7-и блазаров, с красными смещениями больше 2.5, анализируя данные, накопленные с помощью Swift UVOT / XRT и Fermi-LAT. Наблюдается несколько периодов вспышек со значительным увеличением потока и изменением фотонного индекса в высокоэнергетическом γ -диапазоне для PKS 1830-211 ($z = 2.507$), LQAC 247-061 ($z = 2.578$), TXS 0536+145 ($z = 2.690$) и 4C+41.32 ($z = 2.550$). PKS 1830-211 был в чрезвычайно ярком состоянии на MJD 58596,49, когда средний поток за 3 дня увеличился до $(1.74 \pm 0.04) \cdot 10^{-5} \text{ photon cm}^{-2} \text{ s}^{-1}$. Рентгеновское излучение PKS 1830-211 также сильно изменчиво и характеризуется фотонным индексом в диапазоне 0.34-0.94. Для моделирования усредненного во времени широкополосного спектрального распределения энергии рассматриваемых источников, мы использовали однозонный лептонный механизм излучения, когда для обратного комптоновского рассеяния учитываются как синхротронные, так и внешние фотоны. В результате были оценены соответствующие параметры излучающих частиц, а также энергетика струи.

Ключевые слова: механизмы излучения: нетепловой: рентгеновские лучи:
 γ -лучи: блазары

REFERENCES

1. P.Padovani, D.M.Alexander, R.J.Assef et al., Rev. Astron. Astrophys., **25**, 2, 2017.
2. M.Ackermann, R.Anantua, K.Asano et al., Astrophys. J. Lett., **824**, L20, 2016.
3. L.Foschini, G.Ghisellini, F.Tavecchio et al., Astron. Astrophys., **530**, 77, 2011.
4. L.Foschini, G.Ghisellini, F.Tavecchio et al., Astron. Astrophys., **555**, 138, 2013.
5. K.Nalewajko, Mon. Not. Roy. Astron. Soc., **430**, 9, 2013.
6. A.Brown, Mon. Not. Roy. Astron. Soc., **431**, 824, 2013.

7. *B.Rani, T.P.Krichbaun, L.Fuhrmann et al.*, *Astron. Astrophys.*, **552**, A11, 2013.
8. *S.Saito, L.Stawarz, Y.T.Tanaka et al.*, *Astrophys. J.*, **766**, 11, 2013.
9. *M.Hayashida, K.Nalewajko, G.M.Madejski et al.*, *Astrophys. J.*, 807, 79, 2015.
10. *A.Shukla, K.Mannheim, S.Patel et al.*, *Astrophys. J.*, **854**, L26, 2018.
11. *C.M.Urry, P.Padovani*, *Publ. Astron. Soc. Pacif.*, **107**, 803, 1995.
12. *P.Giommi, P.Padovani*, *Mon. Not. Roy. Astron. Soc.*, **2268**, L51–L54, 1994.
13. *A.Abdou, M.Ackermann, M.Ajello et al.*, *Astrophys. J.*, **710**, 810, 2010.
14. *G.Ghisellini, L.Maraschi, A.Treves*, *Astron. Astrophys.*, **146**, 204, 1985.
15. *S.D.Bloom, A.P.Marscher*, *Astrophys. J.*, **461**, 657, 1996.
16. *L.Maraschi, G.Ghisellini, A.Celotti*, *Astrophys. J.*, **397**, L5, 1992.
17. *M.Biazejewski, M.Sikora, R.Moderski et al.*, *Astrophys. J.*, **545**, 107, 2000.
18. *G.Ghisellini, F.Tavecchio*, *Mon. Not. Roy. Astron. Soc.*, **397**, 985, 2009.
19. *M.Sikora, M.Begelman, M.Rees*, *Astrophys. J.*, **421**, 153, 1994.
20. *C.Dermer, R.Schlickeiser*, *Astrophys. J.*, **416**, 458, 1993.
21. *C.Dermer, R.Schlickeiser, A.Mastichiadis*, *Astron. Astrophys.*, **256**, L27–L30, 1992.
22. IceCube Collaboration, *Science*, **361**, 147, 2018.
23. *P.Padovani, P.Giommi, E.Resconi et al.*, *Mon. Not. Roy. Astron. Soc.*, **480**, 192, 2018.
24. *A.Mücke, R.Protheroe*, *Astroparticle Physics*, **15**, 121, 2001.
25. *K.Mannheim*, *Astron. Astrophys.*, **269**, 67, 1993.
26. *K.Mannheim, P.L.Biermann*, *Astron. Astrophys.*, **221**, 211, 1989.
27. *A.Mücke, R.Protheroe, R.Engel et al.*, *Astroparticle Physics*, **18**, 593, 2003.
28. *M.Böttcher, A.Reimer, K.Sweeney et al.*, *Astrophys. J.*, **54**, 768, 2013.
29. *S.Ansoldi, L.A.Antonelli, C.Arcaro et al.*, *Astrophys. J.*, **863**, L10, 2018.
30. *A.Keivani, K.Murase, M.Petropoulou et al.*, *Astrophys. J.*, **864**, 16, 2018.
31. *K.Murase, F.Oikonomou, M.Petropoulou*, *Astrophys. J.*, **865**, 124, 2018.
32. *N.Sahakyan, V.Baghmany, D.Zargaryan*, *Astron. Astrophys.*, **614**, A6, 2018.
33. *C.Righi, F.Tavecchio, L.Pacciani*, *Mon. Not. Roy. Astron. Soc.*, **484**, 2067, 2019.
34. *M.Cerruti, A.Zech, C.Boisson*, *Mon. Not. Roy. Astron. Soc.*, **483**, L12, 2019.
35. *N.Sahakyan*, *Astron. Astrophys.*, **622**, A144, 2019.
36. *S.Gao, A.Fedynitch, W.Winter et al.*, *Nat. Astron.*, **3**, 88, 2019.
37. *N.Sahakyan, P.Giommi*, *Mon. Not. Roy. Astron. Soc.*, **513**, 4645, 2022.
38. *S.Abdollahi, F.Acero, L.Baldini*, *Astrophys. J. Suppl. Ser.*, **260**, 53, 2022.
39. *N.Sahakyan, D.Israyelyan, G.Harutyunyan et al.*, *Mon. Not. Roy. Astron. Soc.*, **498**, 2594, 2020.
40. *W.B.Arwood, A.A.Abdou, M.Ackermann et al.*, *Astrophys. J.*, **697**, 1071, 2009.
41. *S.Gasparyan, N.Sahakyan, V.Baghmany et al.*, *Astrophys. J.*, **863**, 114, 2018.
42. *D.Zargaryan, S.Gasparyan, V.Baghmany et al.*, *Astron. Astrophys.*, **608**, A37, 2017.
43. *V.Baghmany, S.Gasparyan, N.Sahakyan*, *Astrophys. J.*, **848**, 111, 2017.
44. *R.J.Britto, E.Bottacini, B.Lott et al.*, *Astrophys. J.*, **830**, 162, 2016.

45. *P.Giommi, M.Perri, M.Capalbi et al.*, Mon. Not. Roy. Astron. Soc., **507**, 5690, 2021.
46. HI4PI Collaboration, Astron. Astrophys., **594**, A116, 2016.
47. *P.M.W.Kalberla, W.B.Burton, D.Hartman et al.*, Astron. Astrophys., **440**, 775, 2005.
48. *J.M.Dickey, F.J.Lockman*, Ann. Rev. Astron., **28**, 215, 1990.
49. *Y.L.Chang, C.H.Brandt, P.Giommi*, Astron. Astrophys, **30**, 100, 2020.
50. *N.Sahakyan, D.Israyelyan, G.Harutyunyan et al.*, Mon. Not. Roy. Astron. Soc., **517**, 2757, 2022.
51. *N.Sahakyan, S.Gasparyan*, Mon. Not. Roy. Astron. Soc., **470**, 2861, 2017.
52. *G.Ghisellini, F.Tavecchio*, Mon. Not. Roy. Astron. Soc., **448**, 1060, 2015.
53. *E.Massarò, A.Tramacere, M.Perri et al.*, Astron. Astrophys., **448**, 861, 2006.
54. *A.Tramacere, P.Giommi, M.Perri*, Astron. Astrophys., **501**, 879, 2009.
55. *A.Tramacere, E.Massarò, A.Taylor*, Astrophys. J., **739**, 66, 2011.
56. *A.Tramacere*, Astrophys. Source Code Library, ascl:2009.001, 2020.